Pergamon

Int. J. Heat Mass Transfer. Vol. 40, No. 18, pp. 4405–4423, 1997

Printed in Great Britain
0017-9310/97 $17.00+0.00

PII: S0017-9310(97)00064-1

A three-dimensional simulation of coupled turbulent flow and macroscopic solidification heat transfer for continuous slab casters

S. H. SEYEDEIN and M. HASAN†

Department of Mining and Metallurgical Engineering, McGill University, 3450 University St, Montreal, Quebec, Canada H3A 2A7

(*Received* 14 *November* 1996 *and in final form* 1 *February* 1997)

Abstract—A numerical investigation was conducted for exploring the steady state transport phenomena of turbulent flow, heat transfer and macroscopic solidification in a continuous stainless steel slab caster. The numerical model is based on a generalized transport equation applicable to all the three regions, namely liquid, mushy and solid, which exist in a slab caster. The turbulence effects on the transport equations were taken into account using a low-Reynolds number k–ε turbulence model. The solidification of molten steel was modeled through the implementation of the popular enthalpy–porosity technique. A control volume based finite-difference scheme was used to solve the modeled equations on a staggered grid arrangement. A series of simulations was carried out to investigate the effects of the casting speed, the delivered superheat and the immersion depth of the twin-ported submerged entry nozzle (SEN) on the velocity and temperature distributions and on the extent of the solidified and mushy regions on the narrow and broad faces of the caster. In the absence of any known experimental data related to velocity profiles in a slab caster, the numerical predictions of the solidified profile on a caster's narrow face were compared with limited experimental data and a good agreement was found. © 1997 Elsevier Science Ltd.

1. INTRODUCTION

Over the last two decades, there have been intensive research activities undertaken worldwide related to various aspects of continuous casting (CC) processes for slab, billet and bloom casters. In spite of these studies, an advanced mathematical model, which can enhance the quantitative and qualitative understanding of the process, is still not available. Mathematical models can play a major role in the optimization of the casting parameters, e.g. mold and spray cooling systems. Modeling of a CC process is concerned with the liquid–solid phase change problems in which three-dimensional turbulent convective heat transfer in liquid side has an important effect on the growth of the solidified steel shell. Thus, a realistic model for a CC process should be capable of simulating coupled turbulent fluid flow, heat transfer and solidification.

Although flows in commercial CC processes for liquid steel are often turbulent and recirculatory in nature, a very few number of investigators have considered the effect of turbulence in their studies. Asai and Szekely [1] considered a two-dimensional model for a continuous billet casting system. The turbulent flow in the liquid zone was modeled using the one-equation turbulence model (Kolmogrov–Prandtl model) and the computations of the flow field within the mushy zone were carried out on the variable viscosity model. A less satisfactory agreement between measurements and predictions in their study clearly reveals the weakness of the one-equation turbulence model in the calculation of the flow field of a continuous billet caster.

Thomas and co-workers, in a series of papers [2–4], investigated the effect of superheat dissipation on the fluid flow and temperature fields in a continuous-slab casting system. They solved both the three-dimensional and two-dimensional governing momentum and energy equations within the liquid pool. These studies did not couple the process of solidification with the fluid flow and heat transfer within the caster. First, the fluid flow and temperature fields were obtained and later the rate of heat transfer at the wall was used in the one-dimensional solidification model in order to find the rate of growth of the solidifying shell. Since these studies were carried out for a single phase material, the interactions among liquid, mushy and solid phases were not appropriately considered.

Flint [5] reported the results of the heat transfer and fluid flow of the three-dimensional simulation of a continuous slab caster. He utilized a commercial code (PHOENICS) and said to have solved the momentum and enthalpy equations and claimed to have implicitly accounted for the solidification process. He cited that the turbulence behavior of the fluid was modeled using the standard high Reynolds k–ε turbulence model. The application of this turbulence model requires a separate wall function

† Author to whom correspondence should be addressed.

NOMENCLATURE

A D'arcy coefficient
a_P, a_{nb}, b coefficients in the discretized governing equations
c_1, c_2, c_μ empirical constants for low Reynolds turbulent methods
c_p specific heat
C morphology constant
D nozzle hydraulic diameter
D_k extra dissipation term in k-equation
E_ε extra generation term in ε-equation
f_1, f_2, f_μ empirical constants for low Reynolds turbulent methods
f_l liquid fraction
G turbulent kinetic energy generation in k-equation
h sensible heat
H total heat (sensible heat and latent heat)
k turbulent kinetic energy
K' permeability
P Pressure
Pr laminar Prandtl number
Re Reynolds number
Re_t turbulent Reynolds number based on the turbulent quantities
S source term
S_Φ source term associated with Φ
T temperature
T' fluctuation of temperature
T_{in} inlet temperature
T_l liquidus temperature
T_s solidus temperature
u_i velocity component in the ith direction; corresponding to u, v and w
$\bar{u}_i$ time-average velocity component in ith direction
u_i' fluctuation of velocity in ith direction
u_{in} inlet velocity
u_s casting speed.

Greek symbols
ΔH nodal latent heat
ΔH_f latent heat of fusion
ε turbulent kinetic energy dissipation rate
γ convective heat transfer coefficient
Γ_Φ diffusion coefficient associated with Φ value
μ laminar viscosity
μ_e effective viscosity equal to $\mu + \mu_t$
μ_t turbulent viscosity
Φ generalized dependent variable
ρ mass density
σ_l laminar Prandtl number
σ_t turbulent Prandtl number
σ_k, σ_ε empirical constants in turbulent model equations.

Superscripts
* non-dimensional variables
— time-averaged variables
′ fluctuation of variables.

approximation at the vicinity of the solid boundary. In a solidification process, the implementation of the near wall functions at the liquid–solid interface is very difficult since the interface is unknown *a priori*. It is not clear from the paper how the wall functions were implemented.

Recently, Choudhary and Mazumdar [6, 7] have reported the two-dimensional modeling results of fluid flow, heat transfer and solidification for continuous steel billet casters. One of the major weaknesses of their model is the fact that they have used an empirical bulk effective viscosity expression to calculate the turbulent eddy-diffusivity in the liquid pool and in the mushy region. The used empirical viscosity expression does not have any rational basis as far as the modeling of a continuous casting process is concerned. These authors have also arbitrarily divided the computational domain into a mold and a submold region. In the submold region, the turbulence level was believed to be 50% of the mold region and accordingly the effective viscosity value was reduced by the same percentage point. The authors themselves have clearly stated the weakness of their model in which the differential turbulence model cannot be applied on a zonal basis since appropriate boundary conditions are unknown at the junction of the zones. The modeling approach of these authors, apart from being two-dimensional, cannot be applied to a continuous slab caster because it lacks fundamental basis, especially with respect to the modeling of turbulence phenomena.

Very recently, one of the present authors (MH), along with his colleague (RG) and a former graduate student (MRA) [8], carried out a two-dimensional numerical study to model couple turbulent flow, heat transfer and macroscopic solidification in the mold and submold regions of a stainless steel slab caster. In a later work [9], these authors extended their coupled turbulent flow and solidification heat transfer model by incorporating the macrosegregation of carbon and taking into account the trajectory of inclusions. They applied their extended model to simulate various transport processes that prevail in round and square billet casters. In both of their works, they applied a

modified version of the Launder and Sharma low-Reynolds k–ε model to analyze the effects of turbulence on transport processes in the liquid and mushy regions. They also employed the enthalpy–porosity method to model fluid flow and solidification in the mushy region. Although the assumption of two-dimensional modeling is applicable for a round billet caster, it limits the applicability of the model for square billet and slab casters. In real continuous billet and slab casting systems, the transport processes are essentially three-dimensional in nature and a two-dimensional model can therefore predict unsatisfactory results.

On the basis of the above literature survey, one can make the following observations:

1. The implementation of the turbulence model in the liquid–solid region, especially in the presence of mushy zone solidification, is still a challenge to be tackled.
2. Most of the previous studies are related to either one or two dimensions. To model a real slab casting system, a three-dimensional study of the fully coupled momentum, energy and solidification is required.

Thus, the present study is concerned with the development of a comprehensive model for the prediction of coupled three-dimensional turbulent flow, heat transfer, and macroscopic solidification in a continuous-slab casting process for steel.

2. MATHEMATICAL MODELING

Figure 1 shows the computational domain along with the physical coordinates system used for a continuous casting machine. In a typical CC machine molten steel flows due to gravity from a holding tundish down through a submerged entry nozzle to a water-cooled oscillatory mold. The primary function of the mold is to extract sufficient heat from the steel, so that the solidified shell at the mold exit is thick enough and strong enough to hold the liquid steel without bulging or breaking. As the solidifying strand exits the mold it then enters a spray cooling zone. The function of the spray zone is to continue to extract heat from the solidifying section.

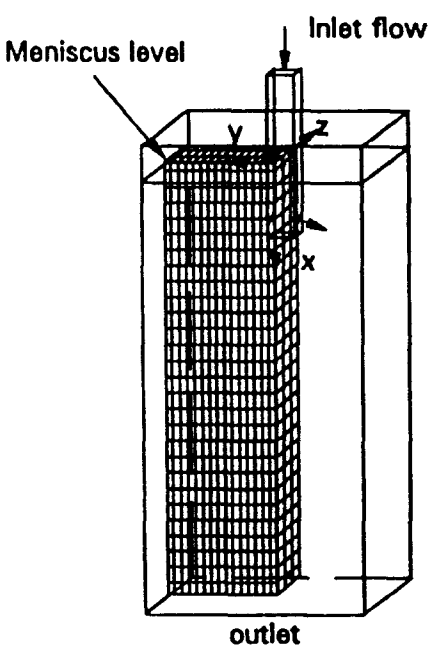

Fig. 1. A schematic view of the caster's domain modeled along with grid distributions and coordinates system used.

In the present study, a twin-ported submerged entry nozzle (SEN) is considered to be a tube of rectangular cross-section having horizontal outlet ports. The nozzle was considered to be inside the computational domain. As a result, the transport equations for the nozzle zone were simultaneously computed (although the results are not shown in this paper) with those applicable for the rest of the domain.

Due to the physical properties of steel in continuous casting machine and the magnitude of the liquid velocity involved, the fluid flow in this process is essentially in turbulent regime. For example, in continuous casting of a slab with a width of 1.27 m, thickness of 0.25 m and casting speed of 0.02 m s^{-1}, the Reynolds number in the nozzle zone with 0.06×0.06 m cross-section becomes greater than 100,000. Therefore, one of the complexities involved in the simulation of a CC process is that the effect of turbulence on the transport processes must be taken into account. The other complexity involved is the modeling of mushy region solidification in the presence of turbulent recirculating bulk motion of the melt.

2.1. *Assumptions of modeling*

The following assumptions were made in the formulation of the mathematical model:

1. With respect to the fixed laboratory frame of reference, the casting process is at steady state and can be represented by the steady, three-dimensional turbulent Navier–Stokes and energy transport equations.
2. Molten steel behaves as an incompressible Newtonian fluid.
3. The top surface of the melt is flat and is maintained at a fixed level. The top surface is also covered with a protective slag layer which keeps the surface thermally insulated from the surroundings.
4. The caster is perfectly vertical with respect to the gravitational field and the curvature of the strand is ignored.
5. The effects of mold taper and mold oscillations are not considered.
6. Equilibrium solidification prevails within the caster and there is negligible segregation of solutes.
7. Thermophysical properties of steel are invariant

and the density and thermal conductivity of the solid phase are equal to those of the liquid phase.

8. Heat release due to solid–solid transformation (viz. $\delta \rightarrow \gamma$ etc.) is not taken into consideration. Only the evolution of latent heat due to solid–liquid phase change is taken into account.
9. In the mold region equi-axed solidification occurs, while below the mold columnar–dendritic solidification takes place.

2.2. *Modeling of the various aspects involved*

Turbulent modeling. In modeling turbulent flows, the Navier–Stokes equations are assumed to be valid when instantaneous velocities are used rather than the time-averaged velocities. Since mathematics cannot handle such instantaneous quantities, they are split into a time average value and a fluctuating term. Using index notation, the time-averaged form of the turbulent transport equations for a single phase can be written as:

Continuity:

$$\frac{\partial(\rho\bar{u}_i)}{\partial x_i} = 0. \tag{1}$$

Momentum equation:

$$\frac{\partial(\rho\bar{u}_i\bar{u}_j)}{\partial x_j} = -\frac{\partial\bar{P}}{\partial x_i} + \frac{\partial}{\partial x_j}\left[\mu\left(\frac{\partial\bar{u}_i}{\partial x_j} + \frac{\partial\bar{u}_j}{\partial x_i}\right) - \rho - \rho\overline{u_i'u_j'}\right]. \tag{2}$$

Energy equation:

$$\frac{\partial(\rho\bar{u}_j\bar{H})}{\partial x_j} = \frac{\partial}{\partial x_j}\left(K\frac{\partial\bar{T}}{\partial x_j} - \rho\overline{u_j'H'}\right). \tag{3}$$

The averaged equations contain the Reynolds stress terms $\rho\overline{u_i'u_j'}$ and the turbulent heat flux $\rho\overline{u_j'H'}$; their determination requires the introduction of a turbulence model.

Most of the general models are based upon the eddy–viscosity approach which was first introduced by Boussinesq at the end of the last century. Accordingly, the Reynolds stress can be rewritten as the function of the turbulent viscosity as:

$$\rho\overline{u_i'u_j'} = -\mu_t\left(\frac{\partial\bar{u}_i}{\partial x_j} + \frac{\partial\bar{u}_j}{\partial x_i}\right) + \frac{2}{3}\delta_{ij}k \tag{4}$$

where μ_t is turbulent viscosity analogous of the molecular viscosity, μ_l, and $k = \frac{1}{2}(\overline{u_i'u_i'})$ is the turbulent kinetic energy per unit mass and the Kroneiker delta δ_{ij} assumes the following form:

$$\delta_{ij} = \begin{cases} 0 & \text{when } i \neq j \\ 1 & \text{when } i = j \end{cases}. \tag{5}$$

Similarly, an eddy diffusivity concept is used to relate the turbulent heat flux to the local mean temperature gradient as:

$$\frac{1}{c_p}\rho\overline{u_j'H'} = -\frac{\mu_t}{\sigma_t}\frac{\partial\bar{T}}{\partial x_j} \tag{6}$$

where, σ_t is the turbulent Prandtl number.

Boussinesq's hypothesis does not provide a complete model for turbulence by itself, because there remains the determination of μ_t. Different turbulence models have been presented based on the additional PDE's required for the definition of μ_t. These models can be classified as zero equation models, one-equation models, and two-equation models.

Two-equation k–ε *model.* One of the most popular turbulent models is the two-equation k–ε model. The first form of this model was proposed by Harlow and Nakayama [10]. They suggested that:

$$\mu_t = \rho c_\mu \frac{k^2}{\varepsilon} \tag{7}$$

where ε is the rate of dissipation of turbulent kinetic energy and c_μ is a function of the turbulent Reynolds number which is a constant value for high Reynolds number flows. A detailed derivation of the turbulent dissipation rate and turbulent kinetic energy equations is available in the literature (Warsi [11]). The steady state equations for k and ε in high Reynolds number k–ε model are as follows:

$$\frac{\partial(\rho\bar{U}_jk)}{\partial x_j} = \frac{\partial}{\partial x_j}\left[\left(\mu_l + \frac{\mu_t}{\sigma_k}\right)\frac{\partial k}{\partial x_j}\right] + \mu_t\left(\frac{\partial\bar{U}_i}{\partial x_j} + \frac{\partial\bar{U}_j}{\partial x_i}\right)\frac{\partial\bar{U}_i}{\partial x_j} - \rho\varepsilon \tag{8}$$

$$\frac{\partial(\rho\bar{U}_j\varepsilon)}{\partial x_j} = \frac{\partial}{\partial x_j}\left[\left(\mu_l + \frac{\mu_t}{\sigma_\varepsilon}\right)\frac{\partial\varepsilon}{\partial x_j}\right] - c_1\mu_t\frac{\varepsilon}{k}\left(\frac{\partial\bar{U}_i}{\partial x_j} + \frac{\partial\bar{U}_j}{\partial x_i}\right)\frac{\partial\bar{U}_i}{\partial x_j} - c_2\rho\frac{\varepsilon^2}{k}. \tag{9}$$

This model is valid only for a single phase flow and is especially applicable in the region having high turbulent Reynolds number $Re_t = \rho k^2/\mu\varepsilon$, and cannot be applied for the region very close to the wall which possesses low value of turbulent Reynolds number.

To extend the k–ε turbulent model to a laminar sublayer close to a solid wall, a low-Re version of this model was initially proposed by Jones and Launder [12, 13]. In the low-Re k–ε turbulent model, some additional terms were included in the k and ε equations to account for the effects of viscous diffusion of k and ε and anisotropy due to the wall. This method has been successfully used to predict the laminarization of wall boundary layer flows. In addition to Jones and Launder model, other investigators proposed several different models. In the present study, the low-Re k–ε turbulent model developed by Launder and Sharma [14], which was seen to yield better results compared to the different types of low-Re k–ε models examined by Patel *et al.* [15], was employed.

A brief formulation of this model for turbulent

Table 1. Coefficients and empirical constants of low-Re k–ε turbulent model developed by Launder and Sharma

Parameter	Value	Parameter	Value
E_c	$\frac{2\mu\mu_t}{\rho}\frac{\partial^2 \bar{U}_i}{\partial x_j \partial x_k}\frac{\partial^2 \bar{U}_i}{\partial x_j \partial x_k}$	c_μ	0.09
D_k	$2\mu\frac{\partial\sqrt{k}}{\partial x_i}\frac{\partial\sqrt{k}}{\partial x_i}$	c_1	1.44
f_μ	$e^{-3.4/(1+Re_t/50)^2}$	c_2	1.92
f_2	$1-0.3e^{-Re_t^2}$	σ_k	1.0
f_1	1.0	σ_ε	1.3

kinetic energy and rate of energy dissipation is presented below:

$$\frac{\partial(\rho\bar{u}_j k)}{\partial x_j} = \frac{\partial}{\partial x_j}\left[\left(\mu_l + \frac{\mu_t}{\sigma_k}\right)\frac{\partial k}{\partial x_j}\right] + \mu_t\left(\frac{\partial\bar{u}_i}{\partial x_j}+\frac{\partial\bar{u}_j}{\partial x_i}\right)\frac{\partial\bar{u}_i}{\partial x_j} - \rho(\varepsilon + D_k) \quad (10)$$

$$\frac{\partial(\rho\bar{u}_j\varepsilon)}{\partial x_j} = \frac{\partial}{\partial x_j}\left[\left(\mu_l + \frac{\mu_t}{\sigma_\varepsilon}\right)\frac{\partial\varepsilon}{\partial x_j}\right] - c_1 f_1 \mu_t \frac{\varepsilon}{k}\left(\frac{\partial\bar{u}_i}{\partial x_j}+\frac{\partial\bar{u}_j}{\partial x_i}\right)\frac{\partial\bar{u}_i}{\partial x_j} - c_2 f_2 \rho\frac{\varepsilon^2}{k} + E_\varepsilon \quad (11)$$

where

$$\mu_t = \rho f_\mu c_\mu \frac{k^2}{\varepsilon}. \quad (12)$$

The values for E_ε, D_k, f_μ, c_1, c_2, c_μ, f_1, f_2, σ_k and σ_ε for the Launder–Sharma model are listed in Table 1.

Solidification modeling. The solidification of alloys mostly occurs over a temperature range. Therefore, for a binary-alloy solidification in a continuous casting machine, three distinct regions can be distinguished: namely, liquid, solid and mushy regions. In the mushy zone, solid and liquid phases coexist and latent heat of fusion is released during the solidification process. Basically, there are two main approaches for modeling the solidification of pure metal and alloys. They are multiple and single domain methods. In the present study, the solidification was modeled based on the single domain approach which does not require to track the unknown interface. An important feature of the single region formulation is to incorporate the effect of the latent heat release at the solid–liquid interface or mushy region in the energy equation. Among the various fixed domain techniques for taking into account the release of latent are: apparent or effective heat capacity methods, and enthalpy based method. The latter approach was adopted in the present work. In this technique, the total enthalpy is decomposed into the sensible and nodal latent heat in the energy equation:

$$H = h + \Delta H \quad (13)$$

where:

$$h = \int_{T_{ref}}^{T} c_p \, dT \quad (14)$$

and for constant c_p, $h = c_p(T - T_{ref})$. In order to establish the region of phase change, the latent heat contribution is specified as a function of temperature i.e. $\Delta H = f(T)$.

Since the energy equation is valid for the solid, liquid and mushy regions, the nodal latent heat can be related to the liquid fraction. It becomes zero in the solid phase and equals the latent heat of fusion (ΔH_f) in the liquid phase. In the mushy region, latent heat is assumed to be a linear function (or can be any other function) of liquid fraction as:

$$\Delta H = \Delta H_f f_l \quad (15)$$

where f_l is the liquid fraction, which is a function of temperature. The simplest function (linear function) is formulated as follows:

$$f_l = \begin{cases} 1 & \text{when } T \geqslant T_l, \\ \dfrac{T - T_s}{T_l - T_s} & \text{when } T_l \geqslant T \geqslant T_s, \\ 0 & \text{when } T \leqslant T_s. \end{cases} \quad (16)$$

where T_l is the liquidus temperature, and T_s is the solidus temperature.

The final form of the energy equation is obtained by substituting equations (6) and (13) into the energy equation [equation (3)]:

$$\frac{\partial(\rho\bar{u}_j\bar{h})}{\partial x_j} = \frac{\partial}{\partial x_j}\left[\left(\frac{\mu}{Pr}+\frac{\mu_t}{\sigma_t}\right)\frac{\partial\bar{h}}{\partial x_j}\right] - \frac{\partial(\rho\bar{u}_j\overline{\Delta H})}{\partial x_j}. \quad (17)$$

The last term in equation (16) represents the latent heat exchange due to solid–liquid phase change resulting from the turbulent convective flow.

A clarification is needed in the usage of this source term in the present model. One should realize that the present model is based on the assumption that the solid fraction and liquid fraction in the mushy region are moving at the same speed. This assumption can be substantiated by the fact that in a real continuous slab caster, in the upper part, a narrow mushy region seems to develop. This is due to the highly turbulent state of the molten metal from the inlet nozzle flow. In this narrow mushy region, one can assume an equiaxed solidification process to prevail, where an equal velocity in the liquid and solid regions exists. In the lower part of a continuous slab caster, the columnar solidification in the mushy region seems to occur. Due to the decrease in the momentum of the melt, the liquid and solid velocities in the mushy region approach to that of the casting speed. Thus, in the lower part of the caster, one can safely assume that the solid and liquid velocities in the mushy region are equal to the casting speed. On the basis of the above

argument, the general form of the source term $(\partial(\rho\bar{u}_j\overline{\Delta H})/\partial x_j)$ remains the same and can be said to be valid for both upper and lower parts of the caster.

Modeling of fluid flow in the mushy region. There are presently two approaches for modeling of fluid flow in a mushy region, i.e. variable viscosity and D'arcy source methods. Since the first approach suffers from the lack of information about viscosity in a mushy region, in the present study, the second method was adopted to model fluid flow in the mushy region. In this approach, it is assumed that the flow in the mushy region is governed by D'arcy laws for a porous media, i.e.

$$\bar{u}_i = -\frac{K'}{\mu}\left(\frac{\partial P}{\partial x_i} + \rho g_{x_i}\right) \tag{18}$$

where K' is the permeability, which is a function of porosity, or, in the case of a mushy region of a binary alloy, a function of liquid fraction. In this method the permeability is defined in such a manner that when liquid fraction decreases, permeability decreases, and forces all the velocities to zero in the case of a stationary solid. Incorporating the diffusive and convective momentum flux terms, one can write the modified D'arcy equation in the following form:

$$\frac{\partial(\rho\bar{u}_i\bar{u}_j)}{\partial x_j} = \frac{\partial}{\partial x_j}\left[(\mu_l + \mu_t)\frac{\partial \bar{u}_i}{\partial x_j}\right] - S_{C_i} - \frac{\mu}{K'}(u_{i_s} - \bar{u}_i). \tag{19}$$

In the above equation, the coefficient μ/K' decreases from a large value in the solid phase to zero in the liquid phase and consequently the D'arcy source term vanishes as the liquid fraction becomes one. In order to find a suitable function for the permeability of the mushy zone, one should really consider the physics of the solidification process. A well-known expression for obtaining the permeability as a function of liquid fraction for the mushy region can be deduced from the Carman–Koseny equation as follows:

$$\frac{\mu}{K'} = \frac{C(1-f_l)^2}{f_l^3 + q}. \tag{20}$$

The value of C in the above equation depends upon the morphology of the porous media and q is a small positive number introduced to avoid division by zero. In the present work, the value of C has been estimated from the expression given by Minakawa *et al.* [16] as $C = 180/d^2$, where d is assumed to be constant and equal to the secondary dendritic arm spacing. The value of d is of the order of 1×10^{-4} m. A large value of C forces the velocity in the solid region ($f_l = 0$) to be equal to the casting speed, u_{i_s}.

2.3. *Boundary conditions*

The schematic of a slab caster representing the computational domain adopted in this work is shown in Fig. 1. Using two-fold symmetry, the transport equations have been solved for a quadrant of the system as shown in this figure. The grid layout used in computations is also shown in this figure. The following boundary conditions were applied in this simulation:

Inlet boundary condition. All variables were assumed to have a constant value at the inlet of the nozzle.

$$u = u_{in}, \quad v = w = 0, \quad h = h_{in},$$
$$k = 0.01 \times u_{in}^2, \quad \varepsilon = c_\mu k_{in}^{3/2}/0.05D. \tag{21}$$

It is noted that the value of k and ε were selected from semi-empirical equations presented by Lai *et al.* [17].

Free surface. The normal gradient of all variables were set to zero except the velocity perpendicular to the surface which itself was assumed to be zero.

$$\frac{\partial v}{\partial x} = \frac{\partial w}{\partial x} = \frac{\partial k}{\partial x} = \frac{\partial \varepsilon}{\partial x} = \frac{\partial h}{\partial x} = 0 \quad u = 0. \tag{22}$$

Symmetry plane. The same boundary conditions as those of free surface, were used here.

at x–y symmetry plane:

$$\frac{\partial u}{\partial z} = \frac{\partial v}{\partial z} = \frac{\partial k}{\partial z} = \frac{\partial \varepsilon}{\partial z} = \frac{\partial h}{\partial z} = 0 \quad w = 0 \tag{23}$$

at x–z symmetry plane:

$$\frac{\partial u}{\partial y} = \frac{\partial w}{\partial y} = \frac{\partial k}{\partial y} = \frac{\partial \varepsilon}{\partial y} = \frac{\partial h}{\partial y} = 0 \quad v = 0. \tag{24}$$

Outlet. Fully developed conditions were adopted at the outlet, i.e. axial gradients of all dependent variables were assumed to be zero.

$$\frac{\partial u}{\partial x} = \frac{\partial v}{\partial x} = \frac{\partial w}{\partial x} = \frac{\partial k}{\partial x} = \frac{\partial \varepsilon}{\partial x} = \frac{\partial h}{\partial x} = 0. \tag{25}$$

Moving walls. The solidified shell at the moving walls were withdrawn with casting speed. Therefore, the following boundary conditions were employed at these faces:

$$u = u_{c_s}, \quad v = w = k = \varepsilon = 0,$$
$$\frac{\partial h}{\partial y} = \frac{\partial h}{\partial z} = -\frac{\gamma}{K}(h_s - h_a) \tag{26}$$

where γ is the average heat transfer coefficient between the solid surface and the surrounding. In this study, an averaged heat transfer coefficient was used for the mold region and a different averaged heat transfer coefficient was employed in the submold region. The values of the average heat transfer coefficients were taken from the work of Lally *et al.* [18] and are listed in Table 3. It is to be noted that in equation (26) h_s represents the enthalpy at the surface and h_a represents the product of ambient temperature and the specific heat of steel.

Non-dimensionalization of the parameters. In order to profit the advantage of generality, the partial differential equations described above were non-

dimensionalized using the following dimensionless parameters:

$$X=\frac{x}{D},\quad Y=\frac{y}{D},\quad Z=\frac{z}{D},$$

$$U=\frac{u}{u_{\text{in}}},\quad V=\frac{v}{u_{\text{in}}},\quad W=\frac{w}{u_{\text{in}}},$$

$$P^*=\frac{P}{\rho_0 u_{\text{in}}^2},\quad k^*=\frac{k}{u_{\text{in}}^2},\quad \varepsilon^*=\frac{\varepsilon D}{u_{\text{in}}^3},$$

$$h^*=\frac{h}{\Delta H_{\text{f}}},\quad \Delta H^*=\frac{\Delta H}{\Delta H_{\text{f}}},\quad \mu_{\text{t}}^*=\frac{\mu_{\text{t}}}{\mu}, \tag{27}$$

where D is hydraulic diameter of the nozzle, u_{in} is the nozzle's inlet velocity and ΔH_{f} is the latent heat of fusion. It is noted that in the above equations as well as all subsequent equations all overbars for time-averaged quantities have been dropped for simplicity.

Combination of the turbulent and solidification modeling with the Navier–Stokes equations and applying dimensionless parameters [equation (27)] yield to the general form of the governing equation as follows:

$$\frac{\partial(U_i\Phi^*)}{\partial X_i}=\frac{\partial}{\partial X_i}\left(\Gamma_\Phi^*\frac{\partial\Phi^*}{\partial X_i}\right)+S_\Phi^* \quad i=1,2,3. \tag{28}$$

The value of Φ^* and associated value of Γ_Φ^* are given in Table 2.

Non-dimensional boundary conditions. Inlet boundary condition:

$$U=1,\quad V=W=0,\quad h^*=h_{\text{in}}^*,$$

$$k^*=0.01,\quad \varepsilon^*=c_\mu(0.01)^{3/2}/0.05. \tag{29}$$

Free surface:

$$\frac{\partial V}{\partial X}=\frac{\partial W}{\partial X}=\frac{\partial k^*}{\partial X}=\frac{\partial\varepsilon^*}{\partial X}=\frac{\partial h^*}{\partial X}=0\quad U=0. \tag{30}$$

Symmetry plane:

at x–y symmetry plane:

$$\frac{\partial U}{\partial Z}=\frac{\partial V}{\partial Z}=\frac{\partial k^*}{\partial Z}=\frac{\partial\varepsilon^*}{\partial Z}=\frac{\partial h^*}{\partial Z}=0\quad W=0 \tag{31}$$

at x–z symmetry plane:

$$\frac{\partial U}{\partial Y}=\frac{\partial W}{\partial Y}=\frac{\partial k^*}{\partial Y}=\frac{\partial\varepsilon^*}{\partial Y}=\frac{\partial h^*}{\partial Y}=0\quad V=0. \tag{32}$$

Outlet:

$$\frac{\partial U}{\partial X}=\frac{\partial V}{\partial X}=\frac{\partial W}{\partial X}=\frac{\partial k^*}{\partial X}=\frac{\partial\varepsilon^*}{\partial X}=\frac{\partial h^*}{\partial X}=0. \tag{33}$$

Moving walls:

$$U=U_{\text{s}}=u_{\text{s}}/u_{\text{in}},\quad V=W=k^*=\varepsilon^*=0,$$

$$\frac{\partial h^*}{\partial Y}=\frac{\partial h^*}{\partial Z}=-\frac{\gamma D}{K}(h_{\text{s}}^*-h_{\text{a}}^*). \tag{34}$$

For the sake of simplicity in the subsequent sections superscripts (*) sign from all variables are eliminated, while the variables remain non-dimensional.

3. NUMERICAL SOLUTION

The governing equations [equation (28)] associated with the boundary conditions [equation (29)–(34)] were solved numerically using a control-volume based finite difference method. A hybrid-scheme, which is a combination of a central difference scheme and an upwind scheme, was used to discretize convection terms. The numerical solution procedure was based on Patankar's SIMPLE [19] algorithm. The algebraic form of the general governing equation obtained from the discretization of equation (28) can be written as follows:

$$a_{\text{P}}\Phi_{\text{P}}=a_{\text{N}}\Phi_{\text{N}}+a_{\text{S}}\Phi_{\text{S}}+a_{\text{E}}\Phi_{\text{E}}+a_{\text{W}}\Phi_{\text{W}}+a_{\text{T}}\Phi_{\text{T}}+a_{\text{B}}\Phi_{\text{B}}+b_\Phi. \tag{35}$$

The above discretized equation relates the global value of Φ at the node P to its immediate six neighboring nodes E, W, N, S, T and B with local production terms. The coefficients a_{E}, a_{W}, a_{N}, a_{S}, a_{T} and a_{B} are called linking coefficients, which connect each neighbor with the nodal value Φ_{P}.

The discretized equations were solved iteratively using an implicit relaxation technique and employing the well-known line-by-line TDMA solver until a converged solution was obtained. The following convergence criterion was considered in the present computational study:

$$R_\Phi=\sum_{\text{all nodes}}\left|a_{\text{P}}\Phi_{\text{P}}-\sum_{\text{nb}}a_{\text{nb}}\Phi_{\text{nb}}-b\right|. \tag{36}$$

The iteration loop was terminated when the sum of the residuals for each calculated variable were less than 0.01. In order to accelerate the convergence, the governing equations were first solved without invoking solidification by assuming that the temperature at the moving wall is equal to the liquidus temperature. The results obtained from these runs were later used as guessed values for the coupled fluid flow, heat transfer and solidification runs. In this method, converged solutions of the coupled set of equations were obtained using the underrelaxation factor for energy, turbulent kinetic energy and energy dissipation rate of 0.2 or smaller, while for the other variables underrelaxation factor was as high as 0.5.

Calculations were carried out for a grid size of $30\times22\times12$ wherein a non-uniform grid was manually distributed with the finer mesh distributions in the vicinity of the solid walls. To verify the algorithm, numerical tests were performed to ensure that the solutions were grid-independent. An increase in the number of the grids from $30\times22\times12$ to $30\times28\times19$ resulted in a maximum difference of 6% in the solidified shell thickness at the mold exit. This difference

Table 2. Summary of the non-dimensional governing equations for Launder and Sharma version of the low-Re k–ε turbulent model

Equation	Φ^*	Γ^*_Φ	S^*_Φ
Continuity	1	0	0
U-momentum	U	$\frac{1}{Re}(1+\mu_t^*)$	$-\frac{\partial P^*}{\partial X}+\frac{\partial}{\partial X_i}\left(\Gamma^*_\Phi\frac{\partial U_i}{\partial X}\right)-\frac{A^*}{Re}(U-U_s)$
V-momentum	V	$\frac{1}{Re}(1+\mu_t^*)$	$\frac{\partial P^*}{\partial Y}+\frac{\partial}{\partial X_i}\left(\Gamma^*_\Phi\frac{\partial U_i}{\partial Y}\right)-\frac{A^*}{Re}(V-V_s)$
W-momentum	W	$\frac{1}{Re}(1+\mu_t^*)$	$-\frac{\partial P^*}{\partial Z}+\frac{\partial}{\partial X_i}\left(\Gamma^*_\Phi\frac{\partial U_i}{\partial Z}\right)-\frac{A^*}{Re}(W-W_s)$
Kinetic energy	k^*	$\frac{1}{Re}\left(1+\frac{\mu_t^*}{\sigma_k}\right)$	$\frac{G^*}{Re}-\varepsilon^*+\frac{D_k^*}{Re}$
Rate of energy dissipation	ε^*	$\frac{1}{Re}\left(1+\frac{\mu_t^*}{\sigma_\varepsilon}\right)$	$\frac{1}{Re}f_1C_1G^*\frac{\varepsilon^*}{k^*}-C_2f_2\frac{\varepsilon^{*2}}{k^*}+\frac{E_\varepsilon^*}{Re^2}$
Energy	h^*	$\frac{1}{Re}\left(\frac{1}{Pr}+\frac{\mu_t^*}{\sigma_t}\right)$	$-\left(\frac{\partial U\Delta H^*}{\partial X}+\frac{\partial V\Delta H^*}{\partial Y}+\frac{\partial W\Delta H^*}{\partial Z}\right)$

where:

$$Re=\frac{\rho u_{in}D}{\mu}$$

$$G^*=\mu_t^*\left(\frac{\partial U_i}{\partial X_j}+\frac{\partial U_j}{\partial X_i}\right)\frac{\partial U_i}{\partial X_j},\quad D_k^*=2\frac{2\sqrt{k^*}}{\partial X_i}\frac{\partial\sqrt{k^*}}{\partial X_i},$$

$$E_\varepsilon^*=2\mu_t^*\left(\frac{\partial^2U_i}{\partial X_j\partial X_k}\right)\left(\frac{\partial^2U_i}{\partial X_j\partial X_k}\right),\quad f_\mu^*=e^{-3.4/(1+Re_t^*/50)^2},\quad Re_t=Re\frac{k^{*2}}{\varepsilon^*},$$

$$\mu_t^*=ReC_\mu f_\mu^*\frac{k^{*2}}{\varepsilon^*},\quad f_1=1,\quad f_2=1-0.3e^{-Re_t^2},\quad A^*=\frac{C^*(1-f_1)^2}{f_1^3+q},$$

$$C_\mu=0.09,\quad C_1=1.44,\quad C_2=1.92,\quad \sigma_k=1.0,\quad \sigma_\varepsilon=1.3,\quad \sigma_t=0.9$$

in shell thickness was less than 6% further downstream.

4. RESULTS AND DISCUSSION

The casting speed and thermophysical properties of stainless steel 304 used in this simulation are given in Table 3. All results discussed below are for a 0.34 m submergence depth (which is defined as the vertical distance from the meniscus to the center of the outlet ports of the nozzle) of the nozzle unless otherwise stated.

In order to ascertain the effects of the casting speed on the flow patterns and solidification profiles, simulation runs were carried out for two casting speeds viz., 0.02 and 0.015 m s^{-1}. Figures 2 and 3 show the predicted velocity fields, solidus and liquidus isotherms, and temperature contours in three separate plots for the centrally symmetric vertical plane parallel to the wide face of the caster for the aforementioned two casting speeds, respectively. As seen from the velocity fields displayed in these figures, the molten steel, supplied through the submerged entry nozzle, impinges onto the narrow face of the mold. After impingement, the flow is divided into two oppositely directed streams, each of which moves parallel to the narrow face and later forms a large recirculation zone. The upper recirculation flow is confined by the mensicus surface and the wide face of the slab. The lower recirculation flow travels both downstream and towards the wide face of the slab and a portion of it returns towards the submerged entry nozzle. The flow field in the caster thus can be characterized by the location of the centers of the upper and lower recirculation zones and the impingement point. The two turbulent recirculating zones lead to the enhancement of the mass, momentum and energy transport in the upper region of the caster. A comparison of the flow fields for the two different casting speeds shows that an increase in the casting speed results in a minor change of the downward recirculation length. There is, however, a change in the magnitude and shape of the velocity in the axial plane (x–y plane). For example, the axial velocity profile at around a non-dimensional distance of 20 from the top free surface shows that for the lower casting speed, the velocity profile takes a more uniform shape compared to that seen for the higher casting speed. This signifies that, for a

Table 3. Thermophysical properties of steel, geometrical parameters and heat transfer coefficients used for the simulation

Variable	Case A	Case B
Thermal conductivity (liquid or solid)	31 W m^{-1} K^{-1}	26
Specific heat (liquid or solid)	700 J kg^{-1} K^{-1}	720
Latent heat of fusion	264 kJ kg^{-1}	272
Liquidus temperature	1454°C	1531
Solidus temperature	1400°C	1518
Inlet temperature	1470–1490°C	1558
Casting speed	0.01–0.02 m s^{-1}	0.0267
Viscosity	0.007 kg m^{-1} s^{-1}	0.0055
Density	7000 kg m^{-3}	6980
Slab width	1.27 m	1.05
Mold length	0.75 m	0.6
Slab thickness	0.254 m	0.22
Nozzle port width	0.058 m	56
Nozzle port height	0.1 m	45
Caster length simulated	3.0 m	3.0
Nozzle submergence length	0.34–0.23 m	0.1
Heat transfer coefficient in the mold region	1500 W m^{-2} K^{-1}	see ref. 20
Heat transfer coefficient in the submold region	750 W m^{-2} K^{-1}	see ref. 20

higher casting speed, the effect of the impinging liquid steel onto the narrow face of the slab is felt at a greater distance downstream. Moreover, a stronger upward recirculation zone is obtained in the case of a higher casting speed, which leads to an increase of turbulence at the free surface. Figure 4(a) shows the three-dimensional velocity vectors on the two centrally symmetric planes and the top free surface. An enlarged view of the flow pattern for the upper part of the caster is shown in Fig. 4(b). From this figure it is seen that the reverse flow under the submerged nozzle is weak, which can be explained from the nullifying effect between the two oppositely directed flows; the downward flow comes from the free surface and the upward flow is supplied by the lower recirculation flow under the nozzle. The velocity fields in Figs. 2(a) and 3(a) also show that, for both cases, the axial velocity is quite uniform in the downstream region and the liquid steel moves vertically downward in the casting direction.

Liquidus (1454°C) and solidus (1400°C) isotherms in the wide symmetry plane for casting speeds of 0.02 and 0.015 m s^{-1} are shown in Figs. 2(b) and 3(b), respectively. From these figures it is seen that a thinner solidifying shell is obtained within the mold for a higher casting speed. The reason for this is that, at a higher casting speed, the dwelling time of the solidifying shell in the mold decreases and the convective heat transfer between the liquid and solidifying shell increases.

In order to verify the modeling of solidification, an additional run, with parameters specified as case B in Table 3 was carried out. The parameters for this case were taken from the experimental work of Nakato *et al.* [20]. Figure 5 compares the solidified shell thickness predicted at the narrow face by the present model with the measured data of Nakato *et al.* [20]. It is to be noted that the predicted shell presented in this figure is curve-fitted to the data found from the simulation. It can be seen from this figure that for two-thirds of the mold the predicted shell thickness matches the experimental one quite closely. For the last one-third of the mold the shell thickness predicted by our model and the experimental data differs. This discrepancy is due to two factors. First, the experimental data was for a curved mold while our prediction is for a vertical mold. Secondly, although the solidified shell profile on the center of the narrow face along the casting direction was given in Nakato *et al*'s [20] study, neither the experimental heat transfer coefficient nor the experimental heat extraction rate were reported in that paper. In absence of this information we have used in our simulation the standard heat transfer coefficient for the mold region reported by various previous researchers in order to predict the experimental solidified shell profile. In addition to the above, if one considers the measurement uncertainty in Nakato *et al*'s [20] results, the predicted profile in this figure can be said to be in fairly good agreement with the measured solidifying shell.

The effect of the casting speed on the temperature distribution in the liquid region is given in Figs. 2(c) and 3(c), respectively. In both cases molten steel with 26°C superheat (difference between the inlet and liquidus temperatures) is introduced into the mold. For a casting speed equal to 0.015 m s^{-1}, liquid steel loses about 18°C of its superheat upon impingement onto the narrow face of the slab, while for a casting speed of 0.02 m s^{-1} the loss in superheat reduces to 15°C. The available superheat at the impingement area is sufficient enough to remelt the mushy phase, which is seen to develop from the top surface on the mold wall. This phenomena will be described in greater detail in the relevant section which follows. These figures also show that large temperature gradients develop near the solid–liquid interface, while there exists low temperature gradients in the bulk of the melt due to well mixing from the turbulent convective flows. The vari-

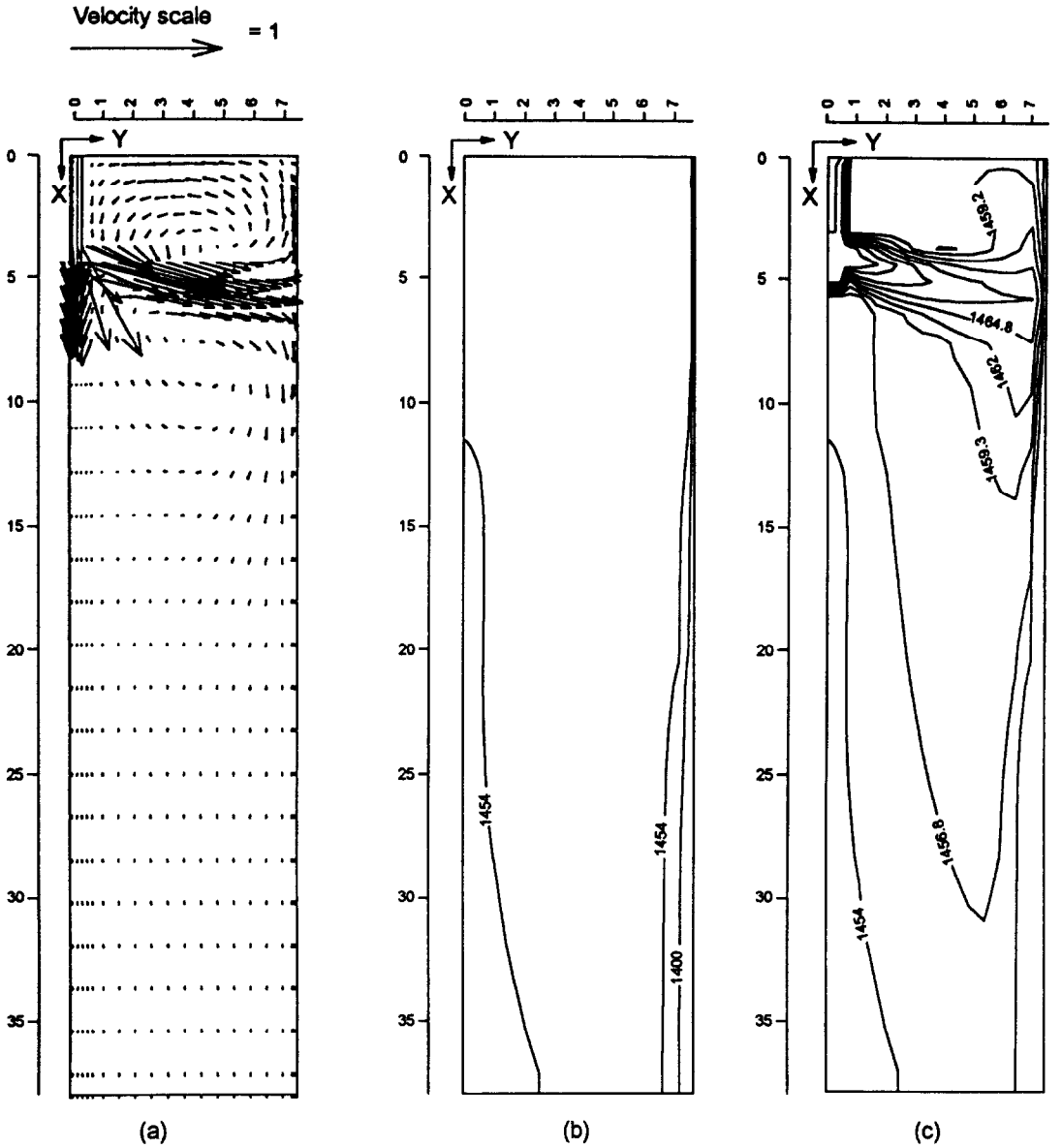

Fig. 2. Computed results at the vertical centrally symmetric plane paralleled to the wide face for a casting speed of 0.02 m s^{-1} and 26°C superheat: (a) velocity vectors, (b) liquidus and solidus isotherms, (c) temperature contours.

ation of the temperature gradient in various parts of the caster is due to the effect of turbulent flow on the heat transfer mechanism. In the region close to the wall, where the turbulence effect disappears, a high heat transfer rate is the manifestation of a high temperature gradient, while far from the liquid–solid interface, where turbulent thermal diffusivity is dominant, the temperature gradient decreases due to intense turbulent mixing. The highest temperature gradient is seen to form near the impingement area on the narrow face of the mold, which in turn illustrates the region of the highest superheat removal and the lowest solidification rate. From the isotherms in Figs. 2(c) and 3(c) it is seen that, at the bottom of the solution domain for $u_s = 0.015$ m s^{-1} the liquid phase almost vanishes, while for the higher casting speed ($u_s = 0.02$ m s^{-1}) the liquid metal is very close to the liquidus temperature. This can be also attributed to the lower dwelling time of the steel for a higher casting speed.

In order to study quantitatively the level of turbulence in the slab caster process, the non-dimensional turbulent viscosity contours on the free surface and two vertically symmetric planes for a casting speed of 0.015 m s^{-1} and 26°C delivered superheat are shown in Fig. 6. In this particular case, the turbulent viscosity varies from zero to 1400 times the molecular viscosity. A zero value of the turbulent viscosity appears in the solidified shell as well as on the submerged nozzle walls, and it increases with the increase of the lateral distance from the solid shell into the bulk liquid phase. The highest value of the turbulent viscosity is observed

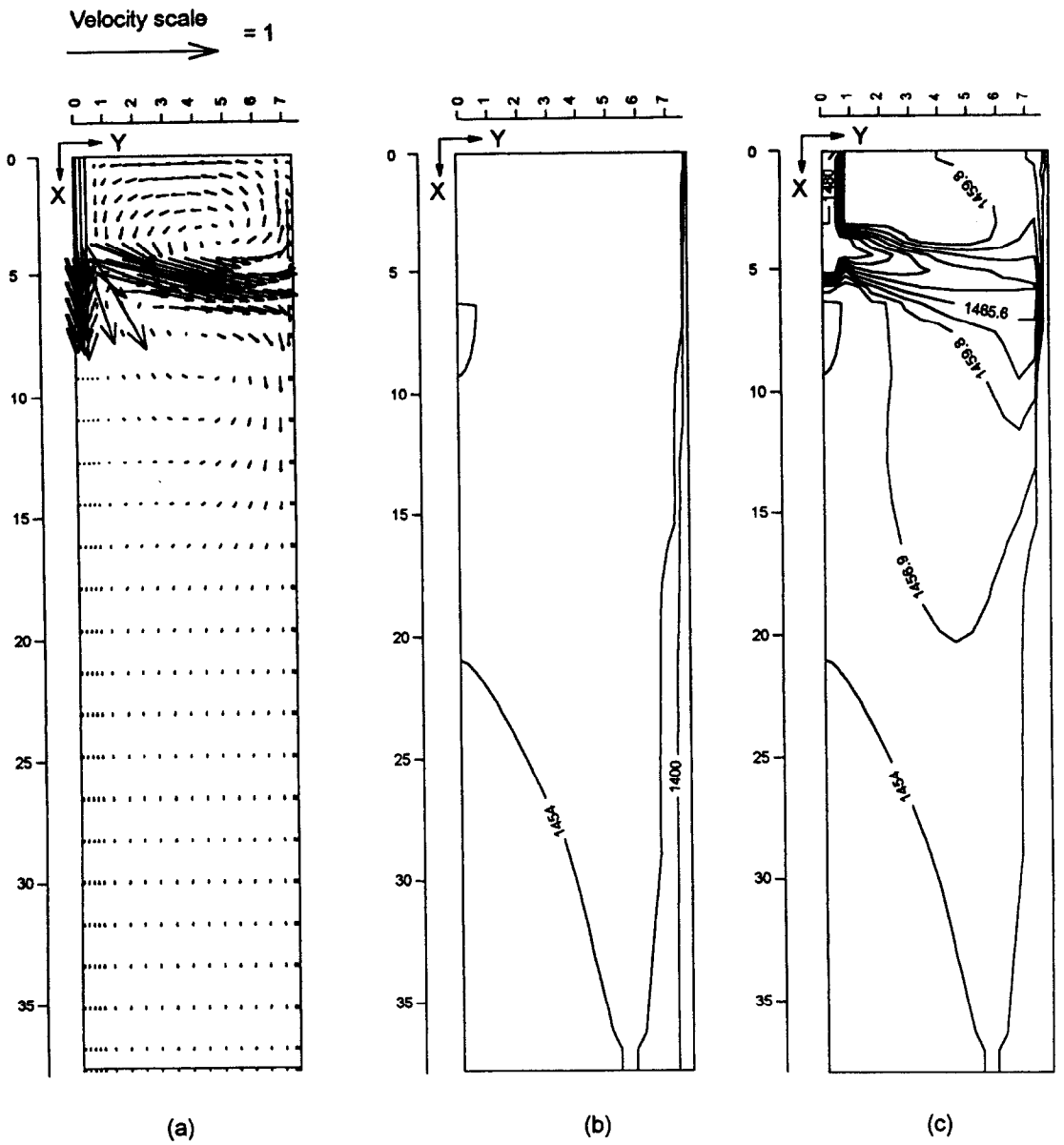

Fig. 3. Computed results at the vertical centrally symmetric plane paralleled to the wide face for a casting speed of 0.015 m s^{-1} and 26°C superheat: (a) velocity vectors, (b) liquidus and solidus isotherms, (c) temperature contours.

under the nozzle, and decreases by expanding the closed loop contours towards solid walls. Due to the wide variations of turbulent viscosity within the caster and considering the fact that the turbulent viscosity is a flow property, it can be concluded that an *ad hoc* viscosity model, which uses an artificially enhanced melt viscosity, cannot be an acceptable modeling approach for the simulation of turbulent flow of molten steel in a continuous-slab casting process.

Figure 7 shows the developments of the solidifying shell and mushy region along the wide and narrow faces of the slab caster for a casting speed of 0.02 m s^{-1} and 26°C inlet superheat at various transverse cross-sectional planes downstream from the top free surface. At non-dimensional axial distance, $x = 0.3$ (0.026 m from the top) a very thin layer of solidified shell is seen to develop on the mold walls. With the downward distance, as more heat is extracted through the solidified shell, the thickness of the solid layer as well as the mushy zone progressively increases. The solid layer and the mushy zone each take almost a round shape around the corner of the mold, which is due to the higher heat extraction rate through the two sides of the mold walls, i.e. heat transfer from both of the transverse directions. The wavy shape of the mushy–liquid interface and remelting of a part of the mushy region, especially at the narrow face of the slab at around $x = 3.4$ is due to the impingement of the superheated liquid steel from the inlet nozzle on to the mold wall. The side streams from this inlet flow are

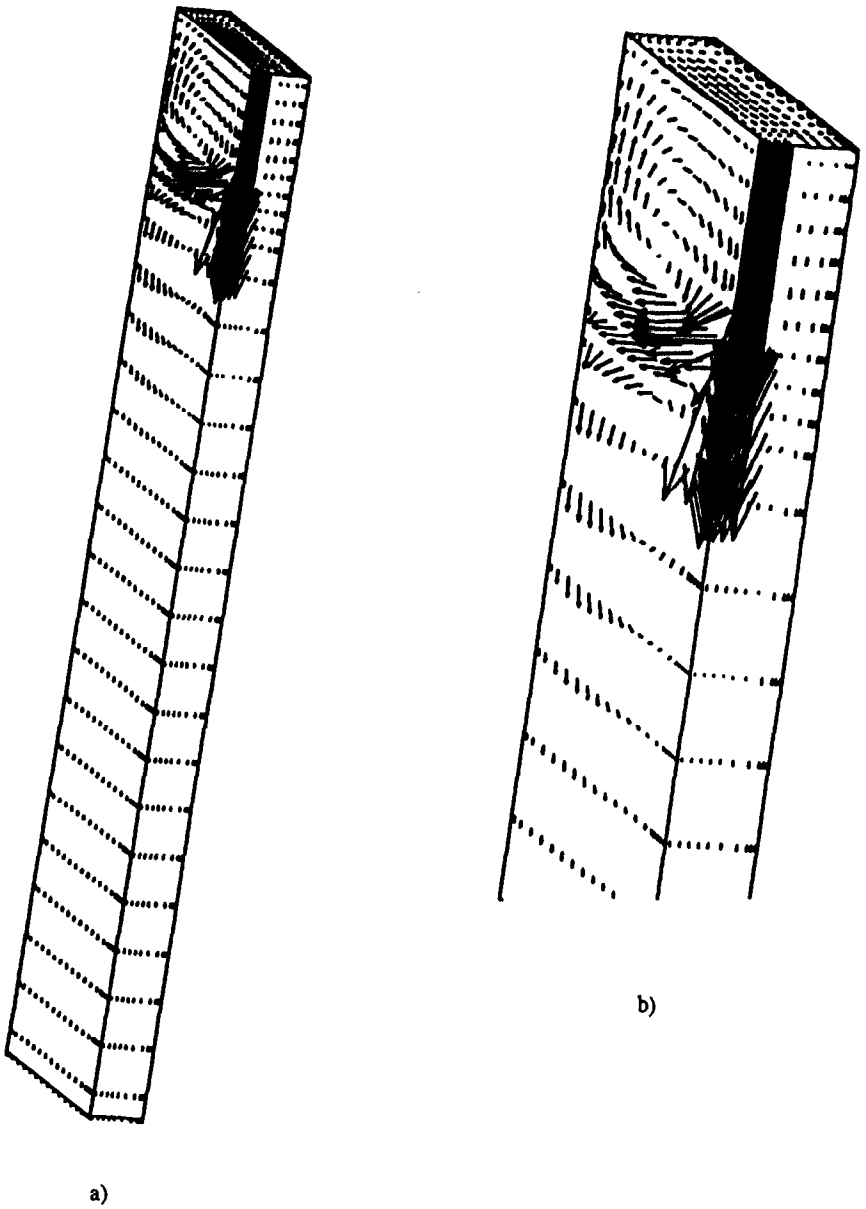

Fig. 4. Three-dimensional surface plot of the velocity vectors for a casting speed of 0.015 m s^{-1} and 26°C superheat; (a) the complete solution domain, (b) enlarged view of the top domain.

responsible for shifting the mushy layer in the direction of the flow. The remelting of the mushy layer reduces the sensible heat of the liquid steel and thus promotes the dissipation of the melt's superheat. It can be seen from these figures that the thickness of the mushy layer at the wide face of the slab caster is maximum at the central symmetric plane. Relatively rapid rate of growth of the solid shell and mushy layer at the center of the wide face, compared to the corresponding growth rate at the wide face close to the narrow side, is due to the fact that the center region is fed essentially by the low superheated melt. This melt comes from the downflow stream of the impinging jet at the narrow face. As the downflow stream moves along the cooled narrow face it loses most of its superheat and moves up through the center of the strand towards the SEN. At further downstream, liquid steel progressively loses its superheat and the growth of the mushy layer on the narrow faces resumes. The decrease of the liquid superheat results in the reduction of the convective heat transfer at the solid–liquid interface, which in turn allows the mushy and solid layers to grow at a faster rate downstream of the strand.

Similar trends in the growth rate of the solidified shell and mushy region as seen in Fig. 7 are also observed for a casting speed of 0.015 m s^{-1} with an inlet superheat equal to 26°C. Figure 8 shows these results in a similar format as Fig. 7. From this figure, it is observed that liquidus isotherm reaches to the

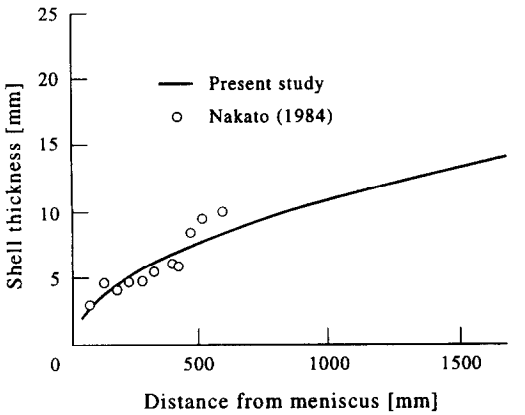

Fig. 5. Comparison of solidified shell thickness predicted in this study (for case B) with experimental data from Nakato *et al.* [20].

wide symmetry plane ($Z = 0$) at around $X = 6$ below the top free surface and returns back further downstream due to remelting. This location coincides with the small dead zone seen under the nozzle, which is influenced by the recirculatory motion of the superheated liquid steel. Further downstream from the free surface, since the liquid temperature is close to the liquidus temperature, the liquid phase region diminishes at a faster rate and vanishes at the exit. For this lower casting speed the solidification rate is also higher compared to the higher casting speed.

In order to study the effect of delivered superheat, Fig. 9 is plotted for the same set of parameters as Fig. 3 except for a superheat of 16°C. A comparison of the Figs. 3(a) and 9(a) show that there is an insignificant effect on the velocity profile due to a change of superheat at 10°C. This change in superheat does not significantly affect the thickness of the solidifying shell, but it does change the extent of the mushy region, especially at the lower part of the caster.

In order to find the effects of the nozzle submergence depth on the flow, temperature and solidification profiles, the model was run for the same set of parameters as for Fig. 3 but with a submergence depth of 0.23 m instead of 0.34 m. The results of this simulation are portrayed in Figs. 10 and 11. A comparison of Figs. 10(a) and 3(a) shows that with the decrease of the immersion depth of the nozzle, the upper counter-clockwise recirculating zone becomes a little stronger while the lower and bigger clockwise recirculating zone becomes weaker. A higher turbulence level at the free surface due to a lower nozzle immersion depth may result in an unwanted entrapment of mold flux within the melt and can significantly affect the quality of the cast. The decrease of the immersion depth results in a corresponding decrease of the impingement point of the jet on the narrow face. A comparison of the liquidus and solidus isotherms in Figs. 10(b) and 3(b) reveals that for a shallower nozzle, the liquid steel dissipates its superheat faster which may be attributed to the higher turbulence mixing in the case of a shallower immersion nozzle. The

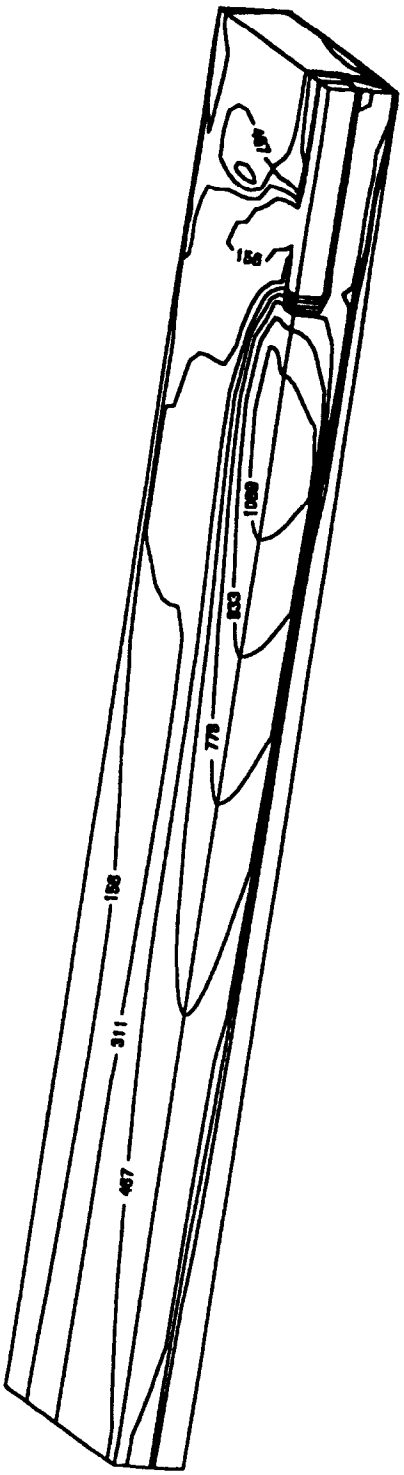

Fig. 6. Three-dimensional surface contour plot of non-dimensional turbulent viscosity for a casting speed of 0.015 m s^{-1} and 26°C superheat.

appearance of the mushy zone across the whole width in the upper part of the submold region is a testimony of the above fact. For a smaller nozzle submergence depth, the liquid steel loses its superheat earlier during its downward flow, a thicker solidified shell is seen to

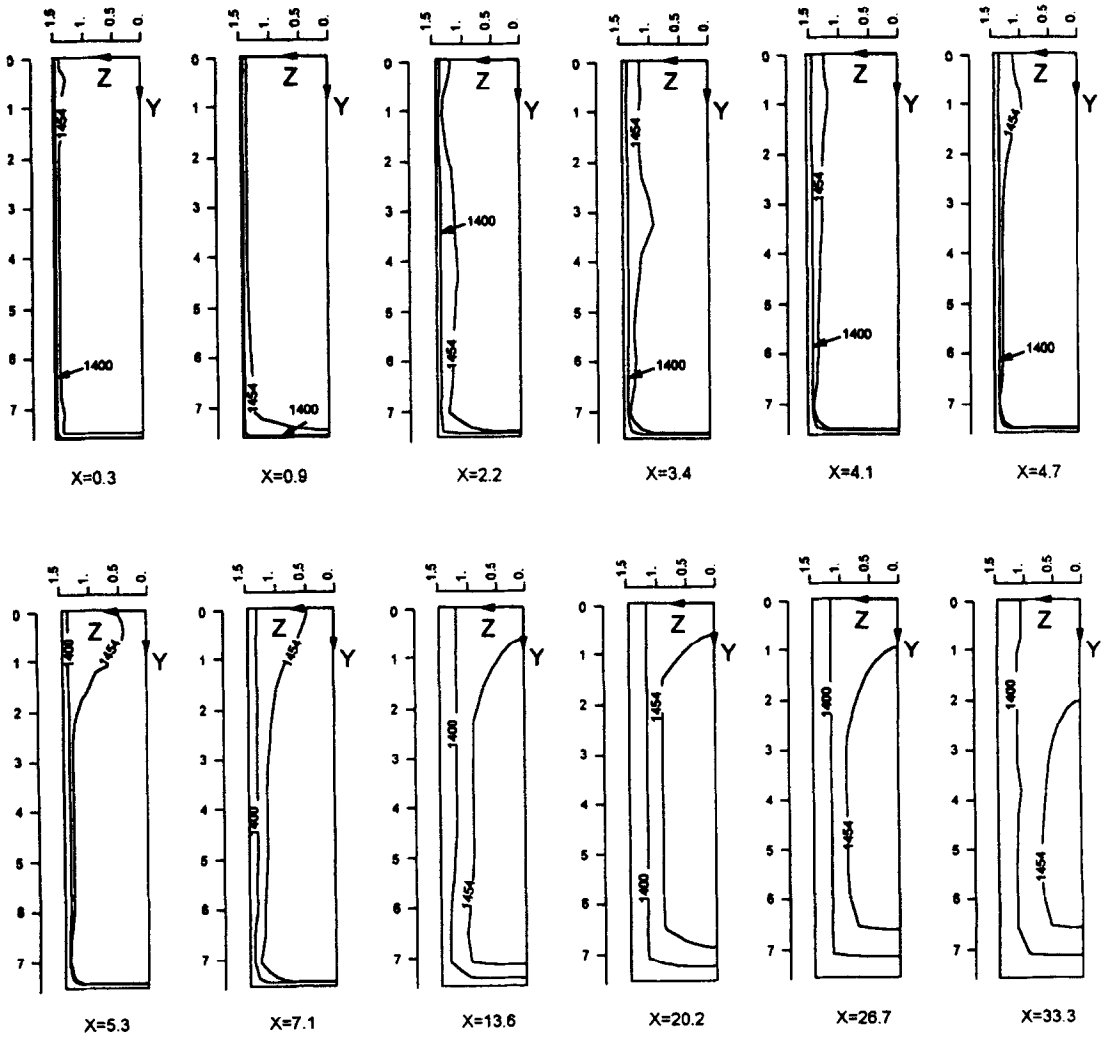

Fig. 7. Contours of solidus and liquidus temperatures at various transverse cross-sectional planes (Y–Z planes) for a casting speed of 0.02 m s^{-1} and 26°C superheat.

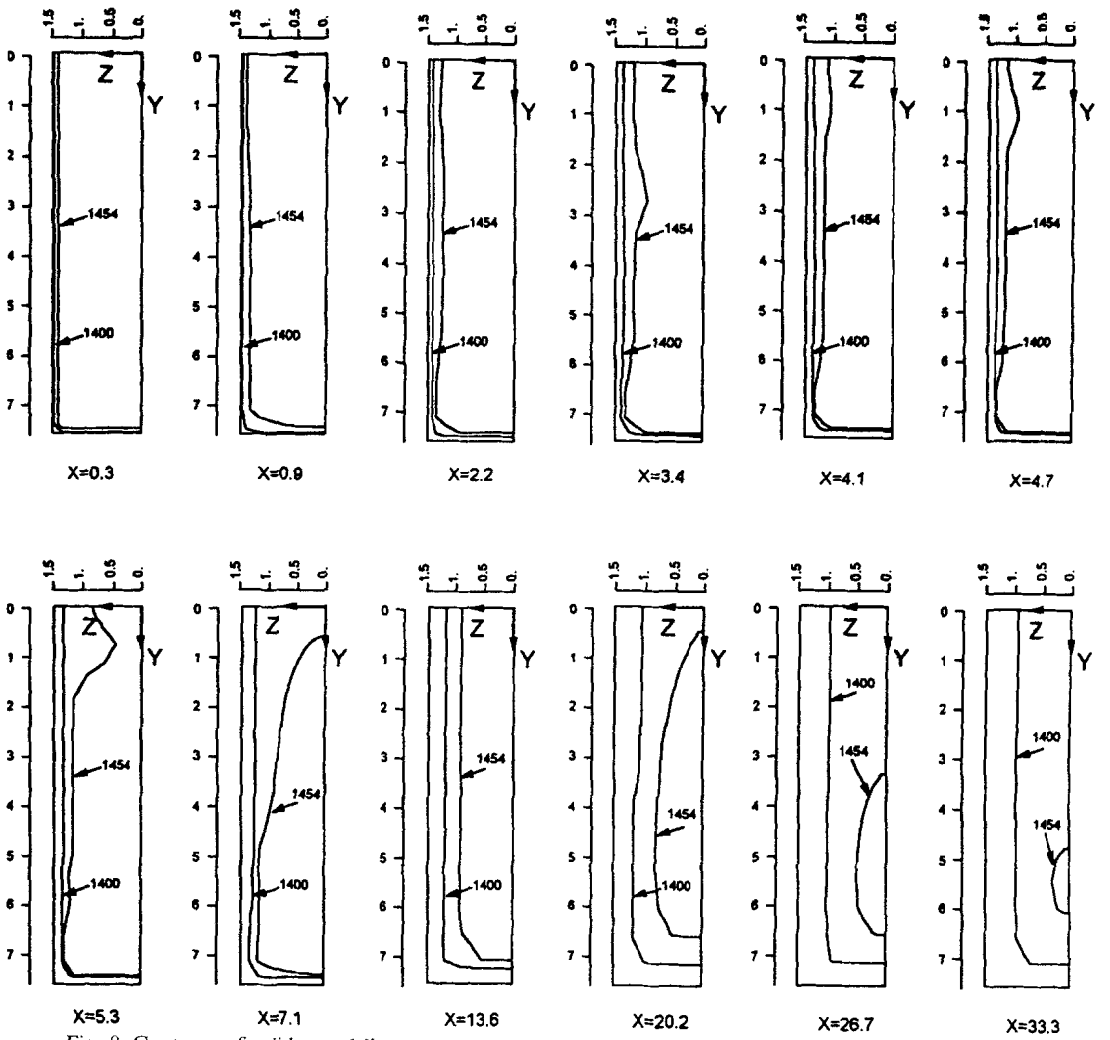

Fig. 8. Contours of solidus and liquidus temperatures at various transverse cross-sectional planes (Y–Z planes) for a casting speed of 0.015 m s^{-1} and 26°C superheat.

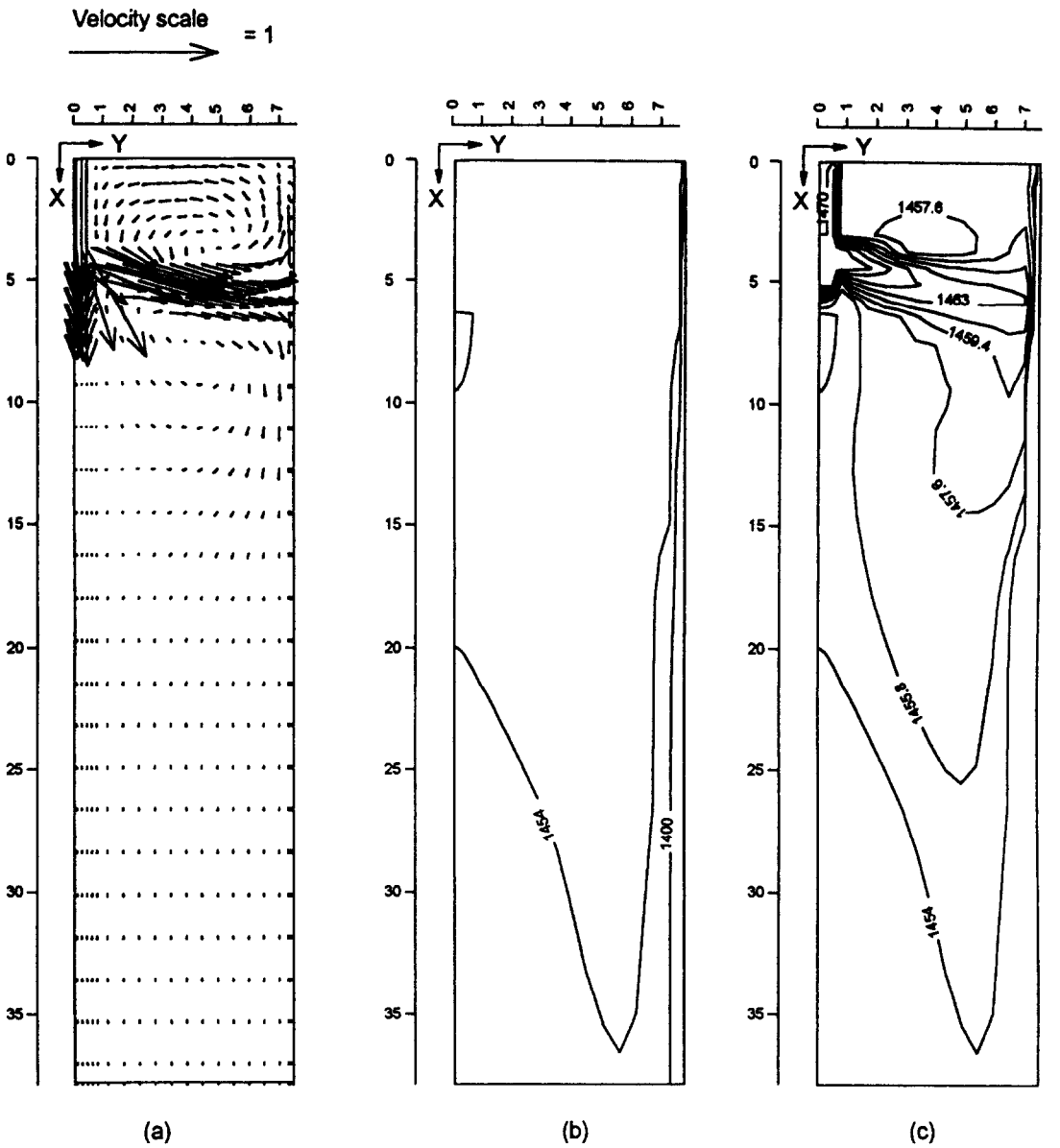

Fig. 9. Computed results at the vertical centrally symmetric plane paralleled to the wide face for a casting speed of 0.015 m s^{-1} and 16°C superheat: (a) velocity vectors, (b) liquidus and solidus isotherms, (c) temperature contours.

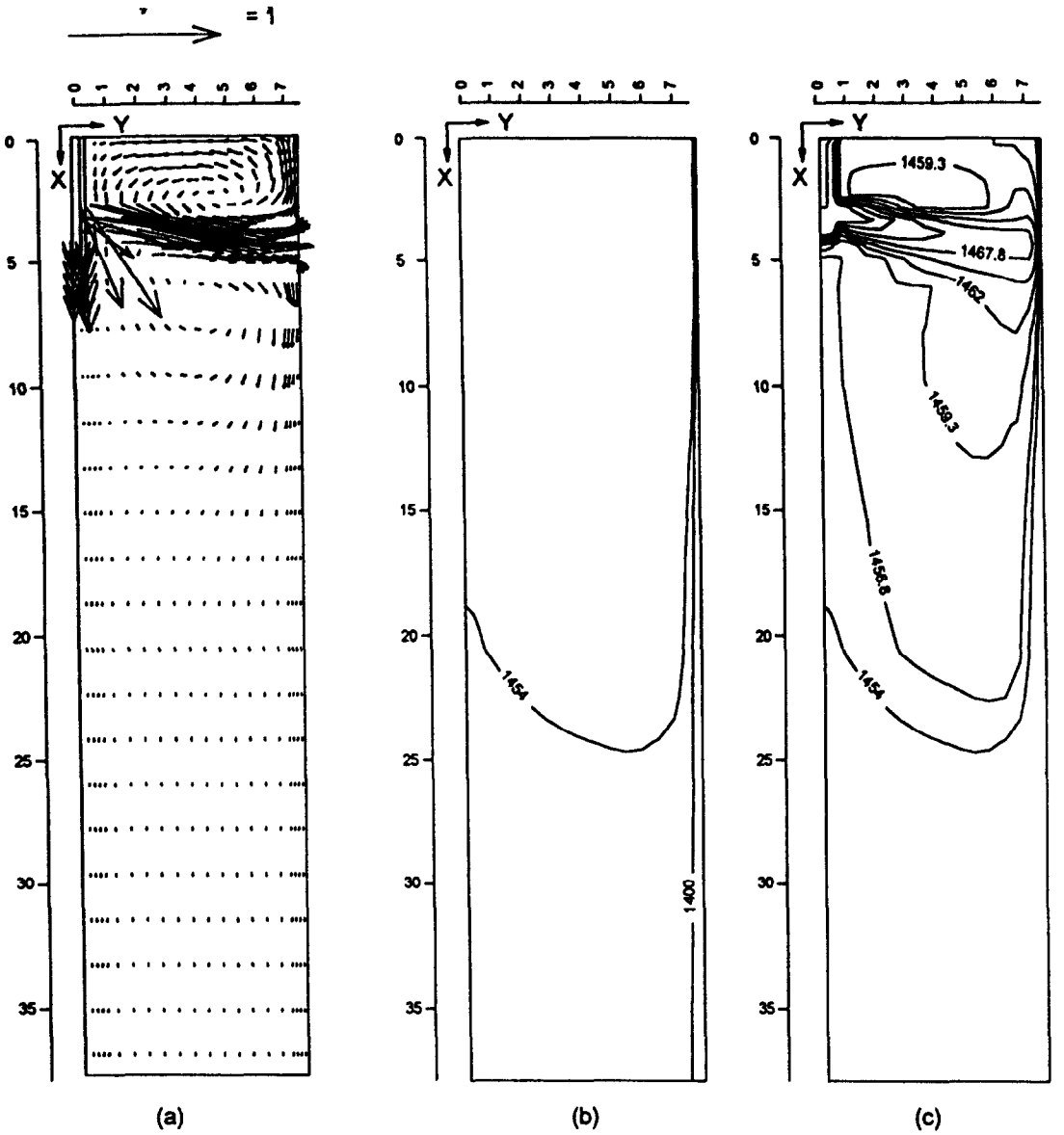

Fig. 10. Computed results at the vertical centrally symmetric plane paralleled to the wide face for a casting speed of 0.015 m s^{-1}, 26°C superheat and SEN = 23 cm; (a) velocity vectors, (b) liquidus and solidus isotherms, (c) temperature contours.

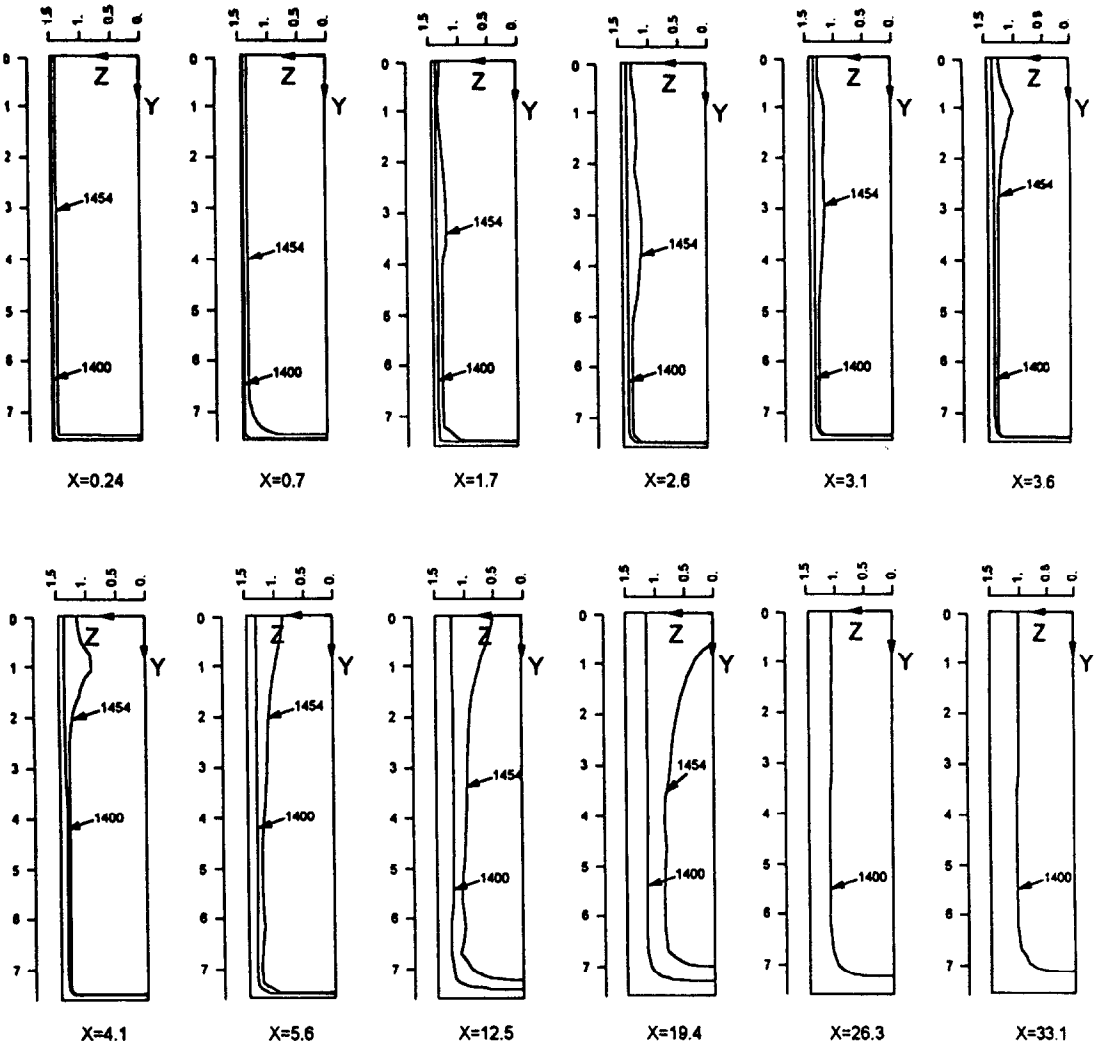

Fig. 11. Contours of solidus and liquidus temperatures at various transverse cross-sectional planes (Y–Z planes) for a casting speed of 0.015 m s^{-1}, 26°C superheat and SEN = 23 cm.

form in the lower part of the caster, which can be seen through a comparison of Figs. 8 and 11.

5. CONCLUDING REMARKS

In this study, a three-dimensional control volume based finite-difference model, along with the associated computer code, have been developed to obtain the numerical solution of the coupled turbulent flow, heat transfer and macroscopic solidification in the mold and submold regions of an industrial size continuous caster for steel slabs. A low Reynolds number k–ε model was used to account for the turbulence effects in the liquid metal and an enthalpy–porosity scheme was employed to model solidification of the mushy region. Numerical accuracy of the model was tested by comparing the predicted solid shell with the only known experimentally measured solidified shell thickness for a slab caster. A very good agreement was obtained between the theoretically predicted and experimentally measured solid shell thickness. By rationally varying the parameters, the model is then used to predict the effect of casting speed, delivered superheat and submergence depth of the nozzle on flow pattern, shell thickness and growth rate of the mushy region, and temperature and turbulent viscosity distributions in the liquid and mushy regions within the caster. The model predicts that most of the inlet superheat is removed in or just below the mold. The model also shows the growth, melting and regrowth of the mushy region at the center of the wide face at a level below the inlet jet impingement region on the narrow face within the mold. Results show a relatively rapid rate of growth of the solid shell and mushy region near the center of the wide face compared to the edges. Results also indicate that, except for the vicinity of the jet impingement region, the inlet superheat has minimal effect on the growth rate of the

solid shell and mushy layer while the casting speed has the most important effect. Except for the central portion of the strand underneath the nozzle, a 50% increase in the casting speed from 0.01 m s^{-1} has shown no change in the turbulence level at the top part of the mold. The nozzle with a smaller submergence depth is seen to enhance the solidification rate, especially in the submold region of the caster. The present study clearly signifies the importance and need for a three-dimensional, conjugate turbulent flow, heat transfer and solidification modeling study for a continuous-slab casting process. Prior modeling studies related to continuous casting processes, which have employed their *ad hoc* effective thermal conductivity or *ad hoc* effective viscosity approach or have uncoupled the process of solidification from heat transfer and fluid flow, cannot provide realistic results, particularly for a slab caster.

REFERENCES

1. Asai, S. and Szekely, J., Turbulent flow and its effects in continuous casting. *Ironmaking and Steelmaking*, 1975, **3,** 205–213.
2. Thomas, B. G., Mika, L. J. and Najjar, F. M., Simulation of fluid flow inside a continuous slab-casting machine. *Metallurgical Transactions B*, 1990, **21B,** 387–400.
3. Thomas, B. G., Najjar, M. F. and Mika, L. J., The removal of superheat from continuous casting moulds. *F. Weinberg International Symposium on Solidification Processing, 29th CIM Conference, Hamilton*, 1990, pp. 131–145.
4. Huang, X., Thomas, B. G. and Najjar, F. M., Modelling superheat removal during continuous casting of steel slabs. *Metallurgical Transactions B*, 1992, **23B,** 339–356.
5. Flint, P. J., A three-dimensional finite difference model of heat transfer, fluid flow and solidification in the continuous slab caster. *Steelmaking Conference Proceedings*, 1990, pp. 481–490.
6. Choudhary, S. K. and Mazumdar, D., Mathematical modelling of transport phenomena in continuous casting of steel. *ISIJ International*, 1994, **34**(7), 584–592.
7. Choudhary, S. K. and Mazumdar, D., Mathematical modelling of fluid flow, heat transfer and solidification phenomena in continuous casting of steel. *Steel Research*, 1995, **66**(5), 199–205.
8. Aboutalebi, M. R., Hasan, M. and Guthrie, R. I. L., Numerical study of coupled turbulent flow and solidification for steel slab casters. *Numerical Heat Transfer Part A*, 1995, **28,** 279–297.
9. Aboutalebi, M. R., Hasan, M. and Guthrie, R. I. L., Coupled turbulent flow, heat, and solute transport in continuous casting processes. *Metallurgical & Materials Transactions*, 1995, **26B,** 731–744.
10. Harlow, F. H. and Nakayama, P. I., Transport of turbulence energy decay rate. Los Alamos Sci. Lab., Report LA-3854, University of California, 1968.
11. Warsi, Z. U. A., *Fluid Dynamics Theoretical and Computational Approaches*. CRC Press, Florida, 1993.
12. Jones, W. P. and Launder, B. E., The prediction of laminarization with two-equation model of turbulence. *International Journal of Heat and Mass Transfer*, 1972, **15,** 301–313.
13. Jones, W. P. and Launder, B. E., The calculation of low-Reynolds-number phenomena with a two-equation model of turbulence. *International Journal of Heat and Mass Transfer*, 1973, **16,** 1119–1130.
14. Launder, B. E. and Sharma, B. I., Application of the energy dissipation model of turbulence to the calculation of flow near a spinning disc. *Letters in Heat and Mass Transfer*, 1974, **1,** 131–138.
15. Patel, V. C., Wolfgang, R. and Scheuerer, J., Turbulence models for near-wall and low-Reynolds-number flows: A review. *AIAA Journal*, 1985, **23**(9), 1308–1319.
16. Minakawa, S., Samarasekera, I. V. and Weinberg, F., Turbulence models for near-wall and low-Reynolds-number flows: a review. *Metallurgical Transactions B*, 1987, **16B,** 245–255.
17. Lai, K. Y. M., Salcudean, M., Tanaka, S. and Guthrie, R. I. L., Mathematical modelling of flows in large tundish systems in steelmaking. *Metallurgical Transactions B*, 1986, **17B,** 449–459.
18. Lally, B., Biegler, L. and Henein, H., Finite difference heat transfer modelling for continuous casting. *Metallurgical Transactions B*, 1990, **21B,** 761–770.
19. Patankar, S. V., *Numerical Heat Transfer and Fluid Flow*. Hemisphere, Washington, DC, 1980.
20. Nakato, H., Ozawa, M., Kinoshita, K., Habu, Y. and Emi, T., Factors affecting the formation of shell and longitudinal cracks in mould during high speed continuous casting of slabs. *Transactions of the Iron and Steel Institute, Japan*, 1984, **24**(11), 957–965.